

Applicability of semiclassical methods for modeling laser-enhanced fusion rates in a realistic settingJohn Jasper Bekx ^{1,*} Martin Louis Lindsey,^{2,3} Siegfried Heinz Glenzer ² and Karl-Georg Schlesinger¹¹*Marvel Fusion, Blumenstraße 28, 80331 Munich, Germany*²*SLAC National Accelerator Laboratory, 2575 Sand Hill Road, MS 72 Menlo Park, California 94025, USA*³*Institute for Computational & Mathematical Engineering, Stanford University, 475 Via Ortega, Stanford, California 94305, USA*

(Received 1 February 2022; accepted 26 April 2022; published 10 May 2022)

In the context of the potential laser-induced enhancement to the rates of DHe³ and DT fusion, we discuss the frequently-used Wentzel-Kramers-Brillouin (WKB) method and the imaginary-time method (ITM). For static external electric fields, we find that these methods predict significant enhancement to the fusion cross section for electric-field strengths $>10^{14}$ V/m, especially at low values (\approx keV) for the enter-of-mass (CoM) energy. When considering dynamic electric fields, this enhancement can be amplified by considering increased photon frequencies. However, we also provide a review of the region of laser-parameter phase space where these semiclassical methods are applicable. We conclude that this allowable region decreases for higher photon frequencies in conjunction with lower values for the electric-field strength, motivating the need for future experiments to test the predictions of these methods and their ranges of validity.

DOI: [10.1103/PhysRevC.105.054001](https://doi.org/10.1103/PhysRevC.105.054001)**I. INTRODUCTION**

Nuclear fusion has the potential of providing a much needed clean source of energy, and with steady technological advances is becoming an ever more approachable goal [1–3]. Fusion is made possible through the process of quantum-mechanical tunneling. Though this process has been discovered and used since around the dawn of quantum mechanics itself [4–8], it is still very elusive in terms of understanding. Fortunately, this has not prevented the scientific community from using it to explain a plethora of observable events, including field ionization, nuclear fusion, and α decay. Though fusion is a ubiquitous process throughout the Universe [9,10], the conditions to achieve nuclear fusion on a terrestrial level, whether through magnetic confinement fusion [11–13] or inertial confinement fusion [14–19], are extremely difficult to achieve. A relatively new avenue to help achieve higher fusion rates is the potential enhancement from high-power lasers.

The effects of a strong external laser field on the tunneling process have been the subject of much research over the last decades [20–38]. The overall consensus has arisen that a strong external laser field has the capability to enhance the tunneling probability. The majority of disagreement originates from how much enhancement can be expected as a function of the laser parameters, such as the intensity, or equivalently the electric-field strength, the photon energy, the temporal profile of the pulse, and the level of coherence. With the advent of increasingly more powerful laser facilities (LCLS [39], SACLA [40], EuXFEL [41,42], PAL-XFEL [43], SwissFEL [44]), the potential laser-induced enhancement to

quantum tunneling, and in particular to fusion reactions, may usher in a new era of laser-fusion science.

The theoretical modeling of the effect of an external laser field on the nuclear process of fusion is very challenging. Researchers frequently resort to perturbative methods, such as a Floquet-like approach (used in, e.g., Refs. [32,34]) or the use of the Kramers-Henneberger (KH) approximation (used in, e.g., Refs. [23,33,35]) or semiclassical approaches, such as the Wentzel-Kramers-Brillouin (WKB) method (e.g., Refs. [30,32,36]) or the imaginary-time method (ITM) (e.g., Refs. [22,30,45]). However, despite numerous theoretical models being used to predict laser-induced fusion enhancement, the present lack of any controlled experimental verification has led to varying conclusions about the practicality of laser-induced enhancement, i.e., whether current-day or near-future laser facilities will allow for observable fusion enhancement. Preceding works have attempted to determine those laser parameters for which a significant enhancement to the transparency, and/or the fusion cross section, would be achieved (see Refs. [32–38]). However, it is never really discussed exactly how much a “significant” enhancement entails, or how much is needed to be experimentally observable. The work of Queisser and Schützhold [32] sets an enhancement in the transparency by one or two orders of magnitude as a goal, whereas the work of Lv *et al.* [33] is satisfied with an increase in the cross section by a factor of around 5. The work of Wang [34] indicates an increase to the cross section by at least an order of magnitude is necessary, whereas the work of Kohlfürst *et al.* [35] considers an order-of-magnitude increase to the tunneling rate. In addition, these estimates are typically made for a fixed set of center-of-mass (CoM) energies, at which enormous enhancements may be highlighted (up to eight to twelve orders of magnitude [32,34,36]). However, on the one hand a large enhancement to an already minute cross section may not be enough for experimental verification,

*Corresponding author: john.bekx@marvelfusion.com

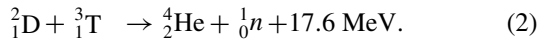
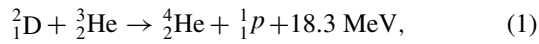
while on the other hand a large enhancement that only persists for a very small range of CoM energies may get “washed away” in an experiment.

In light of this, the goal of this paper is the following: we wish to determine whether the aforementioned and frequently used semiclassical approaches are in fact capable of achieving accurate predictions of laser-enhanced fusion rates in a way that is immediately verifiable by an experiment on a laser-created plasma state [46]. In doing so, we will discern the realm of applicability of these semiclassical methods and comment on their practicality regarding the aforementioned goal. We did not perform a similar analysis for perturbative methods as these are typically used in the literature to obtain qualitative predictions of laser-induced enhancement that justify further research and the use of more sophisticated methods (see, e.g., Refs. [30,32]).

The paper is structured as follows: in Sec. II we elaborate on calculable theoretical quantities of phenomenological relevance. In addition we briefly outline the WKB method and the ITM and apply them to the fusion process in the absence of an external laser field for clarification. Subsequently, we show how to incorporate the relevant laser parameters into these frameworks and discuss their ranges of applicability. In Sec. III we apply these methods to calculate the enhancement in fusion rates stemming from the introduction of both a constant, time-independent (static) electric field and a time-dependent (dynamic) electric field. We also compare with prior theoretical predictions. Section IV provides conclusions and an outlook.

II. THEORY

The fusion reactions that will be considered in this paper are deuterium-helium fusion and deuterium-tritium fusion:



D and T refer to the isotopes ${}^2_1\text{H}$ and ${}^3_1\text{H}$, respectively. In the absence of an external laser field, the fusion cross section is modeled by the phenomenological form [10,16]

$$\sigma(\mathcal{E}) = \frac{S(\mathcal{E})}{\mathcal{E}} \mathcal{T}_{\mathcal{E}}, \quad (3)$$

where \mathcal{E} is the CoM energy of the two fusing particles, $S(\mathcal{E})$ is the astrophysical S factor, which is assumed to be a slowly varying function of \mathcal{E} , and $\mathcal{T}_{\mathcal{E}}$ is the tunneling transparency. The astrophysical S factor for DHe³ and DT fusion used throughout this work was obtained from the work of Bosch and Hale [47] and provides a parametrized form for $S(\mathcal{E})$. This parametrization is valid for CoM energies in the ranges of [0.3,900] and [0.5,550] keV for DHe³ and DT, respectively. The transparency is dominated by its exponential nature and is approximated as [7]

$$\mathcal{T}_{\mathcal{E}} = e^{-\sqrt{\frac{\mathcal{E}_G}{\mathcal{E}}}}, \quad (4)$$

where the Gamow energy $\mathcal{E}_G = 2\mu\pi^2\kappa^2/\hbar^2$, with μ the reduced mass, and $\kappa = e^2 Z_1 Z_2 / (4\pi\epsilon_0)$. The modification to this transparency factor as a result of a high-power laser field

is how the fusion cross section will be enhanced. From the enhanced transparency, the cross section is obtained and this cross section is subsequently used to obtain the reactivity $\langle\sigma v\rangle$, given by [10,16]

$$\langle\sigma v\rangle = \left(\frac{\mu}{2\pi k_B T}\right)^{3/2} \int d^3\mathbf{v} \exp\left(-\frac{\mu}{2k_B T} v^2\right) \sigma(v) v, \quad (5)$$

where k_B is the Boltzmann constant, T is the temperature, \mathbf{v} is the relative velocity of the reduced two-particle system, and $v = |\mathbf{v}|$. As an approximation, a thermal Maxwellian velocity distribution may be assumed, leading to a representation with respect to the CoM energy:

$$\langle\sigma v\rangle = \sqrt{\frac{8}{\mu\pi(k_B T)^3}} \int_0^\infty d\mathcal{E} S(\mathcal{E}) \exp\left(-\sqrt{\frac{\mathcal{E}_G}{\mathcal{E}}} - \frac{\mathcal{E}}{k_B T}\right). \quad (6)$$

In doing so, the relations $\mathcal{E} = \mu v^2/2$ and $d^3\mathbf{v} = 4\pi v^2 dv$ were used. The integral over \mathcal{E} is practically handled by means of a cutoff value. The reactivity is accurate to within an order of magnitude if the cutoff is at least the energy at the Gamow peak, which is the CoM value for which the exponential in the integrand has a maximum, at $\mathcal{E}_{\text{peak}} = (\mathcal{E}_G k_B^2 T^2/4)^{1/3}$. With the reactivity, the total fusion yield can be easily estimated after determining the irradiated volume, which can be obtained provided the laser focus spot size and the density of the target.

In the upcoming semiclassical approaches, the laser-induced modification to the transparency will appear as a direct result from including the external electric field in the potential that is considered. The dynamics of the fusion process are governed by the two-body time-dependent Schrödinger equation (TDSE), which can be reduced to two one-body TDSEs: one for the center-of-mass motion and one for the relative motion. An excellent pedagogical elaboration on obtaining these equations is given by Mişicu and Rizea [23]. We need only concern ourselves with the relative motion, governed by an effective reduced one-body Schrödinger equation, presented in the length gauge:

$$i\hbar \frac{\partial \psi(\mathbf{r}, t)}{\partial t} = \left[-\frac{\hbar^2}{2\mu} \nabla_r^2 + V(r) - eZ_{\text{eff}} \mathbf{r} \cdot \mathbf{E}(t) \right] \psi(\mathbf{r}, t), \quad (7)$$

where \mathbf{r} denotes the relative separation coordinate between the two fusing particles and $V(r)$ describes the Coulomb and nuclear potential in the absence of a laser field. The effective charge is given by $Z_{\text{eff}} = (Z_1 A_2 - Z_2 A_1)/(A_1 + A_2)$, with Z_i and A_i the charge number and atomic number of the i th fusing particle. The electric field is denoted by $\mathbf{E}(t)$. An important note is that this equation is derived by assuming the Coulomb gauge, i.e., the vector potential \mathbf{A} is purely transversal, so that $\mathbf{E}(t) = -\partial\mathbf{A}(t)/\partial t$, and also by assuming the dipole approximation, i.e., $\mathbf{E}(\mathbf{r}, t) \approx \mathbf{E}(t)$. This is a valid approximation so long as the wavelength of the laser field is much larger than the spatial extent of the interacting system, i.e., the extent of the sub-barrier tunneling region. We will use this to place clear restrictions on the applicability of the upcoming models. The reason for employing the length gauge in favor of the more frequently employed velocity gauge (where the $\mathbf{r} \cdot \mathbf{E}(t)$ part is replaced by $\mathbf{p} \cdot \mathbf{A}(t)/\mu$; see, e.g., [23,32,33,36]) is that

this allows us to distinguish between time-independent (static) electric fields and time-dependent (dynamic) electric fields. (In the velocity gauge, a static electric field still implies a dynamic vector potential.)

We emphasize that, as we model a two-body fusion reaction, we are neglecting plasma effects, such as the screening from electrons (briefly discussed in Queisser *et al.* [32]) and the effect of the laser on the velocity distribution of the particles. Our sole focus will be on the enhancement caused by the deformation of the Coulombic potential caused by the external laser field.

We proceed with an outline of the two semiclassical approaches that are employed in this work.

A. Semiclassical approaches

The semiclassical approximation can be made in the case when the action functional $S[\mathbf{q}]$, with \mathbf{q} denoting a set of generalized coordinates, between two spacetime points (\mathbf{q}_a, t_a) and (\mathbf{q}_b, t_b) is much larger than \hbar , i.e.,

$$S[\mathbf{q}] = \int_{t_a}^{t_b} dt L(\mathbf{q}, \dot{\mathbf{q}}, t) \gg \hbar, \quad (8)$$

where the L denotes the Lagrangian $L = T - V$, T being the kinetic energy and V the potential energy. This is equivalent to the transition amplitude between the aforementioned spacetime points being dominated by the contribution of the trajectory, \mathbf{q}_{eom} , which obeys the classical equation of motion, hence the term ‘‘semiclassical.’’ For this trajectory, the Lagrangian obeys the Euler-Lagrange equations, and the action functional, $S[\mathbf{q}]$, reverts to Hamilton’s principle function, $\mathcal{S}(\mathbf{q}_{\text{eom}})$. It can be shown [20,45] that in the semiclassical approximation the transparency can be calculated via

$$\mathcal{T} = e^{-2\text{Im} \mathcal{S}/\hbar}. \quad (9)$$

There are two semiclassical methods we will be employing to calculate the above expression: the Wentzel-Kramers-Brillouin (WKB) method [48,49] and the imaginary-time method (ITM) [45]. For each of these methods, \mathcal{S} is given by

$$\mathcal{S} = \begin{cases} \pm \int_{\text{tunnel}} dr p(r) & \text{for WKB,} \\ \int_{\text{tunnel}} dt [L + \mathcal{E}] & \text{for ITM.} \end{cases} \quad (10)$$

For the WKB method, the imaginary part can be read off by using

$$p(r) = \sqrt{2\mu[\mathcal{E} - V(r)]} = i\sqrt{2\mu[V(r) - \mathcal{E}]}, \quad (11)$$

and the choice in the sign of $\text{Im} \mathcal{S}$ is taken, in conjunction with the integration over the tunneling region, in such a way that the result is positive, ensuring an exponentially decaying behavior in the transparency. For the ITM, L is the conventional Lagrangian and the integration is taken over the time it takes to tunnel through the barrier. Applying the change of coordinate $t = -i\tau$, with $\tau = it$ the imaginary-time coordinate, will

allow for the imaginary part to be easily read off as follows:

$$\begin{aligned} \mathcal{S}_{\text{ITM}} &= \int_0^{t\mathcal{E}} dt \left[\frac{\mu}{2} \left(\frac{\partial r(t)}{\partial t} \right)^2 - V(r(t)) + \mathcal{E} \right] \\ &= \int_0^{-i\tau\mathcal{E}} d(-i\tau) \left[\frac{\mu}{2} \left(\frac{\partial r(\tau)}{\partial(-i\tau)} \right)^2 - V(r(\tau)) + \mathcal{E} \right] \\ &= i \int_0^{-i\tau\mathcal{E}} d\tau \left[\frac{\mu}{2} \left(\frac{\partial r(\tau)}{\partial\tau} \right)^2 + V(r(\tau)) - \mathcal{E} \right]. \end{aligned} \quad (12)$$

Thus, we can see that if the potential does not explicitly depend on t , $r(\tau)$ describes the classical trajectory of a particle moving in the potential $-V$. For a time-dependent potential, the change in coordinate $t = -i\tau$ must be done explicitly in the potential as well, but can perfectly well be treated with the ITM. Conversely, the standard WKB method does not consider time dependence and is ill suited for time-dependent potential barriers. Time-dependent extensions of the WKB method do exist [32,50–52] and are in principle rather straightforward to implement. However, in doing so one arrives at a set of coupled ODE equations, for which it is not clear what initial conditions ought to be imposed when integrating for the solution (see Refs. [50–52]). An excellent review is provided in Ref. [52]. In light of this, we will not employ the WKB method for time-dependent electric fields. This was part of the reason for desiring a clear distinction between static and dynamic electric fields and preferring the length gauge in our modeling of the laser field. We highlight ahead of our results that the WKB method and ITM agreed with each other in both the field-free and the static-field configurations, as will be shown in Secs. II B and III A, respectively.

Let us clarify the use of these approaches by recovering the transparency in the absence of an external electric field.

B. Field-free transparency

In the absence of an external electric field, the potential that defines the barrier under which the fusing particles must tunnel is given by

$$V_l(r) = \frac{\kappa}{r} + \frac{\hbar^2 l(l+1)}{2\mu r^2}, \quad (13)$$

where l denotes the azimuthal quantum number. This potential only accounts for $r \in [R, \infty)$, where R denotes the length scale below which the strong nuclear force dominates over the Coulomb potential and is taken to be $R = 1.44(A_1^{1/3} + A_2^{1/3})$ [16]. Below this value, we assume a constant, flat nuclear potential well. Note that the centrifugal term (dependent on l) is a positive contribution to the potential. The larger l is, the larger the potential barrier through which to tunnel becomes. For that reason, it is common to only consider $l = 0$, for which the tunneling is most probable. Thus, we are working with $V(r) = \kappa/r$. For two fusing particles with a CoM energy \mathcal{E} , the tunneling barrier is defined by the region $R \leq r \leq R_{\mathcal{E}}$, where R is equal to 3.891 fm for both DHe³ and DT and the classical turning point $R_{\mathcal{E}} = \kappa/\mathcal{E}$ is defined by the condition $V(R_{\mathcal{E}}) = \mathcal{E}$.

WKB. To calculate the field-free transparency in the WKB approximation, we wish to calculate, from Eq. (9),

$\mathcal{T}_\mathcal{E} = \exp(-2 \text{Im } \mathcal{S}_\mathcal{E}/\hbar)$ with [Eqs. (10) and (11)]

$$\text{Im } \mathcal{S}_\mathcal{E} = \int_R^{R_\mathcal{E}} dr \sqrt{2\mu \left(\frac{\kappa}{r} - \mathcal{E} \right)}, \quad (14)$$

where the integration limits have preemptively been switched to ensure a positive result. In this case, the integral can be evaluated analytically (see, e.g., Ref. [48]), and results in

$$\text{Im } \mathcal{S}_\mathcal{E} = \sqrt{2\mu\mathcal{E}} \left[R_\mathcal{E} \cos^{-1} \left(\sqrt{\frac{R}{R_\mathcal{E}}} \right) - \sqrt{R(R_\mathcal{E} - R)} \right]. \quad (15)$$

Making the approximation $R/R_\mathcal{E} \ll 1$, this can be reduced to

$$\begin{aligned} \text{Im } \mathcal{S}_\mathcal{E} &\approx \sqrt{2\mu\mathcal{E}} \left[\frac{R_\mathcal{E}\pi}{2} - 2\sqrt{RR_\mathcal{E}} \right], \\ \lim_{R \rightarrow 0} \text{Im } \mathcal{S}_\mathcal{E} &\rightarrow \sqrt{2\mu\mathcal{E}} R_\mathcal{E} \frac{\pi}{2}. \end{aligned} \quad (16)$$

With $R_\mathcal{E} = \kappa/\mathcal{E}$, the last expression recovers the Gamow energy from the value of $-2 \text{Im } \mathcal{S}_\mathcal{E}/\hbar$ as

$$-\frac{2}{\hbar} \sqrt{2\mu\mathcal{E}} R_\mathcal{E} \frac{\pi}{2} = -\sqrt{\frac{2\mu\kappa^2\pi^2}{\hbar^2\mathcal{E}}} = -\sqrt{\frac{\mathcal{E}_G}{\mathcal{E}}}, \quad (17)$$

revealing that the Gamow form for the transparency [Eq. (4)] is the result of applying the WKB method with the additional assumption of $R = 0$ [7].

ITM. To calculate the field-free transparency in the ITM approximation, we wish to calculate $\mathcal{T}_\mathcal{E} = \exp(-2 \text{Im } \mathcal{S}_\mathcal{E}/\hbar)$, with

$$\mathcal{S}_\mathcal{E} = \int_0^{i\mathcal{E}} dt \left[\frac{\mu \dot{r}^2(t)}{2} - \frac{\kappa}{r(t)} + \mathcal{E} \right]. \quad (18)$$

To find the required sub-barrier solutions for $r(\tau)$ and $\dot{r}(\tau)$ in imaginary time τ , we solve for the classical equations of motion in the sub-barrier region with a sign-flipped potential:

$$\mu \ddot{r}(\tau) = -\frac{d}{dr} \left(-\frac{\kappa}{r(\tau)} \right) = -\frac{\kappa}{r^2(\tau)}, \quad (19)$$

with the boundary conditions $r(0) = R_\mathcal{E}$ and $\dot{r}(0) = 0$. This is simply Kepler's problem, if we were to redefine $\kappa = Gm_1m_2$, which has been extensively studied and for which a parametrized solution is available:

$$\begin{cases} r(\xi) = R_\mathcal{E} \cos^2 \frac{\xi}{2}, \\ \tau(\xi) = \frac{R_\mathcal{E}}{2} \sqrt{\frac{\mu}{2\mathcal{E}}} (\xi + \sin \xi), \end{cases} \quad (20)$$

for $0 \leq \xi \leq \xi_F < \pi$ and $r(\xi_F) = R$. Note that $R \rightarrow 0$ is equivalent to $\xi_F \rightarrow \pi$. One can check that this solution satisfies the original equation of motion, Eq. (19), and additionally find that $\dot{r}(\xi) = -(2\mathcal{E}/\mu)^{1/2} \tan(\xi/2)$. As such, we obtain

$$\begin{aligned} \mathcal{S}_\mathcal{E} &= i \int_0^{-i\tau_\mathcal{E}} d\tau \left[\frac{\mu}{2} \left(\frac{dr(\tau)}{d\tau} \right)^2 + V - \mathcal{E} \right] \\ &= i\mathcal{E} \int_0^{-i\tau_\mathcal{E}} d\tau \left[\frac{4}{1 + \cos \xi} - 2 \right], \end{aligned}$$

$$\begin{aligned} \text{Im } \mathcal{S}_\mathcal{E} &= 2\mathcal{E} \left[\frac{\xi_F}{2} \sqrt{\frac{2\kappa^2\mu}{\mathcal{E}^3}} - \tau_\mathcal{E} \right] \\ &= \sqrt{\frac{\mu\mathcal{E}}{2}} R_\mathcal{E} [\xi_F - \sin \xi_F], \end{aligned} \quad (21)$$

where the tunneling time is $\tau_\mathcal{E} = \tau(\xi_F) - \tau(0) = \tau(\xi_F)$. The ITM exactly recovers the WKB exponent if we assume $R/R_\mathcal{E} \ll 1$. This can be easily seen by using $\xi_F = 2 \arccos(\sqrt{R/R_\mathcal{E}})$, with the approximation $\arccos(x) \approx \pi/2 - x$ for small x , and $\sin[2 \arccos(x)] = 2x\sqrt{1-x^2}$. As R is of the order of a few fm and $R_\mathcal{E}$ is of the order of pm for most \mathcal{E} , the WKB method and ITM are practically indistinguishable.

When including the effects of an external electric field in the potential, the relevant integrals will no longer have analytically closed solutions and will instead be evaluated numerically.

C. Accounting for nonzero R

From the previous section, we have seen that the Gamow form that we use to model the fusion cross section [Eq. (3)] is equivalent to a WKB/ITM description in the limit $R = 0$ fm. However, for our upcoming calculations, we wish to keep R nonzero for the reasons that (a) it models a more physically realistic system and (b) the integrands in the WKB and ITM exponents diverge for $r \rightarrow 0$. For their numerical treatment this divergence is kept at bay by keeping R nonzero. However, this choice has two consequences.

First, if R is nonzero, the potential exhibits a maximum at $r = R$ and there exist values of \mathcal{E} that exceed this maximum $V(R)$. In such cases, we are no longer considering quantum tunneling. The requirement that $\mathcal{E} < V(R)$, or equivalently $R < R_\mathcal{E} = \kappa/\mathcal{E}$, sets upper limits on allowable CoM energies \mathcal{E} , which are 750 and 375 keV for DHe³ and DT respectively. This in turn sets upper limits on the temperatures T for which an accurate reactivity estimate is possible. For an order-of-magnitude calculation, we mentioned that the cut-off energy for the reactivity integral should be at least the Gamow peak, at $\mathcal{E}_{\text{peak}} = (\mathcal{E}_G k_B^2 T^2 / 4)^{1/3}$. So, the largest allowable temperatures for reactivity estimates become $k_B T \approx 600$ keV and $k_B T \approx 450$ keV for DHe³ and DT, respectively. This restriction does not arise when assuming $R = 0$ as in that case $R = 0 < R_\mathcal{E}$ for all energies \mathcal{E} . At this point, however, we note that an even stricter restriction occurs for the upper bound of \mathcal{E} by the requirement of $\text{Im } S > \hbar$. For nonzero R , the upper limits on \mathcal{E} become 183 and 66.8 keV, for DHe³ and DT respectively, corresponding to allowable temperatures of up to $k_B T \approx 72$ keV and $k_B T \approx 31$ keV, respectively. Keeping $R = 0$ only reduces the upper bound for DT fusion to a value of 295 keV ($k_B T \approx 295$ keV). For DHe³, $\text{Im } S > \hbar$ remains true for CoM energies up to 1.18 MeV, so the upper bound for DHe³ at $R = 0$ comes from the limitation of the astrophysical S factor, at 900 keV ($k_B T \approx 785$ keV).

Second, keeping R nonzero will induce an error in the cross section from the astrophysical S factor, which must be corrected for in the following way. The astrophysical S factor is obtained in the literature from the Gamow-result for the

tunneling cross section [Eq. (3)]. From experimental values of $\sigma(\mathcal{E})$, a discrete selection of points for $S(\mathcal{E})$ may be inferred, which are subsequently fitted and parametrized [47,53]. However, the obtained fit for $S(\mathcal{E})$ came from using the prior ansatz that the transparency takes on the form $\exp(-\sqrt{\tilde{\mathcal{E}}_G/\mathcal{E}})$, assuming $R = 0$. Thus, to keep R nonzero, we ought to obtain an R -dependent S factor, denoted by $S_R(\mathcal{E})$, from the relation

$$\sigma(\mathcal{E}) = \frac{S_R(\mathcal{E})}{\mathcal{E}} e^{-\sqrt{\tilde{\mathcal{E}}_G(R)/\mathcal{E}}}, \quad (22)$$

where a redefined, R -dependent, Gamow energy can be extracted from the WKB result at nonzero R [Eq. (15)], given by

$$\tilde{\mathcal{E}}_G(R) = \frac{8\mu\kappa^2}{\hbar^2} \left[\cos^{-1} \left(\sqrt{\frac{R}{R_{\mathcal{E}}}} \right) - \frac{R}{R_{\mathcal{E}}} \sqrt{\left(\frac{R_{\mathcal{E}}}{R} - 1 \right)} \right]^2. \quad (23)$$

For comparison of our results to the values in the literature, we ought to parametrize S_R ourselves using the R -dependent ansatz in Eq. (22). However, to avoid this tedious work, we may instead write $S_R(\mathcal{E})$ in terms of the old S factor, denoted as $S_0(\mathcal{E})$, as follows:

$$\frac{S_R(\mathcal{E})}{S_0(\mathcal{E})} = \frac{\sigma(\mathcal{E})\mathcal{E}e^{+\sqrt{\tilde{\mathcal{E}}_G(R)/\mathcal{E}}}}{\sigma(\mathcal{E})\mathcal{E}e^{+\sqrt{\mathcal{E}}_G/\mathcal{E}}} = e^{\sqrt{\tilde{\mathcal{E}}_G(R)/\mathcal{E}} - \sqrt{\mathcal{E}}_G/\mathcal{E}}. \quad (24)$$

If this correction factor is not used, an unphysically large enhancement can already be seen in the reactivity for the field-free case, between the assumptions of $R = 0$ and $R \neq 0$. This is illustrated in Fig. 1. One can see that the erroneous result of $R \neq 0$ with $S_0(\mathcal{E})$ (dashed lines) predicts a consistent unphysical enhancement of around an order of magnitude compared to the conventional usage of the $R = 0$ result with $S_0(\mathcal{E})$ (solid lines). The $R = 0$ result with $S_0(\mathcal{E})$ nearly perfectly coincides with the $R \neq 0$ result corrected with $S_R(\mathcal{E})$ (dotted lines), thus illustrating that, to accurately compare our result with previous literary work, the use of $S_R(\mathcal{E})$ is necessary. Results are only shown up to those temperatures where the reactivity is certain to be within an order of magnitude, corresponding to the temperatures mentioned in the previous paragraph. These values coincide with the cutoff energy used in the reactivity integral, and the fact that they differ explains the slight difference between the $R = 0$ result with $S_0(\mathcal{E})$ (solid lines) and the $R \neq 0$ result corrected with $S_R(\mathcal{E})$ (dotted lines). In cross section calculations, we will use $S_R(\mathcal{E})$ consistently and assume that it remains unaltered when including an external laser field.

In the next section, we show how an external electric field is included in the WKB method and the ITM and go over the relevant laser parameters.

D. Inclusion of an external laser field

When including a *static* external electric field, the potential becomes [Eq. (7)]

$$V_E(r) = \frac{\kappa}{r} - eZ_{\text{eff}} r |\mathbf{E}| \cos \theta, \quad (25)$$

Field-free reactivity; $S_0(\mathcal{E})$ vs $S_R(\mathcal{E})$

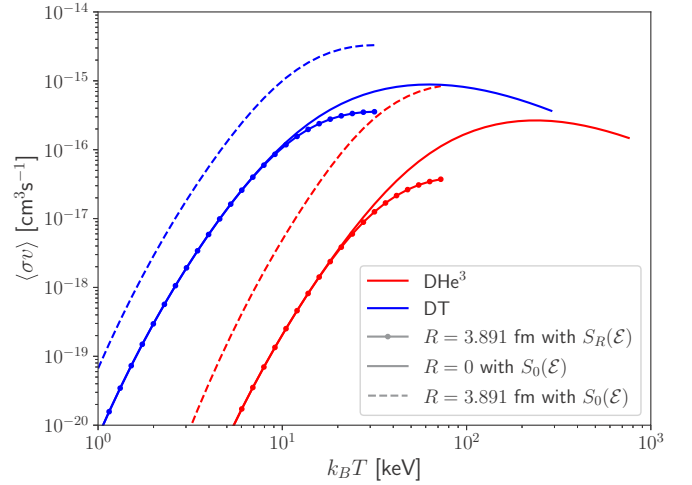


FIG. 1. The field-free reactivity for DHe^3 (red) and DT (blue) fusion. The solid and dashed lines correspond to the WKB result using $S_0(\mathcal{E})$ for the cases of both $R = 0$ (solid) and $R = 3.891$ fm (dashed). The dotted lines refer to the results from WKB for $R = 3.891$ fm using the rescaled $S_R(\mathcal{E})$. The dashed lines illustrate that using a nonzero R in conjunction with $S_0(\mathcal{E})$ may predict unphysical enhancements to the reactivity of up to one order of magnitude as compared the conventional method depicted by the solid lines. Conversely, the agreement between the solid and dotted lines justifies the use of $S_R(\mathcal{E})$ when considering a nonzero R .

where $|\mathbf{E}|$ is the static-field amplitude and $\theta \in [0, \pi]$ defines the angle between the relative particle motion and the polarization direction. Note that $\theta = 0$ or $\theta = \pi$ denote that the polarization of the electric field is in the radially outward or inward direction, respectively. Also, the case $\theta = \pi/2$ is equivalent to the field-free case. For brevity, we will employ the notation $\lambda \equiv eZ_{\text{eff}}|\mathbf{E}|$. In the following formulation, it is assumed that the CoM energy is unaffected by the external field, which enables us to use the same definition of \mathcal{E} from the field-free case. This assumption will also be used for the upcoming dynamical case.

The region under which the fusing particles must tunnel in this case is defined by $r \in [R, R_E]$, where R_E is defined by the condition $\mathcal{E} = V_E(R_E)$, which gives

$$R_E = \frac{-\mathcal{E} \pm \sqrt{\mathcal{E}^2 + 4\kappa\lambda \cos \theta}}{2\lambda \cos \theta}, \quad (26)$$

where only the positive branch recovers $\lim_{|\mathbf{E}| \rightarrow 0} R_E = R_{\mathcal{E}}$. The change in the classical turning point caused by the deformation of the potential is the underlying cause for why laser-induced enhancement (or indeed suppression as we shall see in a bit) is possible. Even though R_E can never become negative, note that it can become complex if $\mathcal{E}^2 < -4\kappa\lambda \cos \theta$. This may occur only when $\cos \theta < 0$ and is an artifact of the employed dipole approximation. The validity in the use of the dipole approximation, requiring $\lambda_{\text{laser}} \gg |R_E - R|$, sets a lower bound on the CoM energy \mathcal{E} for which the approach in this paper is applicable. At large r , the $\lambda r \cos \theta$ part of the potential dominates and can be made arbitrarily

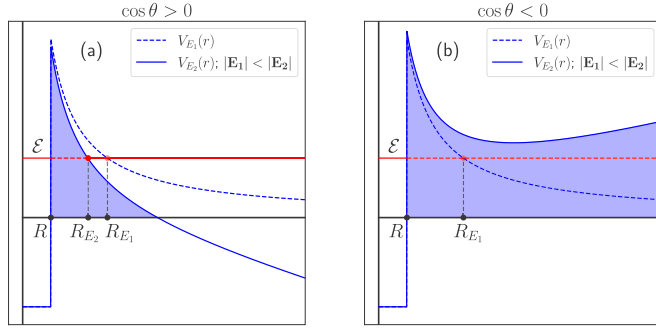


FIG. 2. Schematic static-case illustration of the deformation to the potential, as a function of r , caused by increasing values of $|\mathbf{E}|$ for the cases $\cos \theta > 0$ (a) and $\cos \theta < 0$ (b). In the illustration, the value $|\mathbf{E}_2|$ is larger than $|\mathbf{E}_1|$. The schematic shows that in the case of $\cos \theta > 0$ a classical turning point can always be defined, whereas in the case of $\cos \theta < 0$ this may not always be the case. If a classical turning point can be defined for $\cos \theta < 0$ (by increasing \mathcal{E} or decreasing $|\mathbf{E}|$) a suppression to the fusion cross section is expected compared to the field-free case rather than an enhancement.

and unphysically large. This is shown in Fig. 2, which denotes a schematic of the deformation of the potential $V_E(r)$ to be tunneled through as a function of r for electric-field strengths $|\mathbf{E}_1|$ and $|\mathbf{E}_2|$, with $|\mathbf{E}_1| < |\mathbf{E}_2|$ for $\cos \theta > 0$ (left) and $\cos \theta < 0$ (right). One clearly sees that for higher $|\mathbf{E}|$ values at $\cos \theta > 0$ there will always be an intersection between $V_E(r)$ and \mathcal{E} . Conversely, for $\cos \theta < 0$, the potential may be deformed such that tunneling becomes impossible at the given \mathcal{E} , for which $|R_E - R| \rightarrow \infty$, which obviously violates the use of the dipole approximation. A discussion surrounding the employed approximations and the consequent region of phase space where the semiclassical approaches may be applied will be given in the upcoming Sec. II E. If a classical turning point can be defined for $\cos \theta < 0$ (by increasing \mathcal{E} or decreasing $|\mathbf{E}|$) a suppression to the fusion cross section is expected compared to the field-free case rather than an enhancement. We proceed by calculating the new static-field transparency, $\mathcal{T}_E = \exp(-2 \text{Im } \mathcal{S}_E/\hbar)$, with the WKB method and with ITM.

WKB. To calculate the static-field transparency in the WKB approximation, we wish to calculate

$$\text{Im } \mathcal{S}_E = \int_R^{R_E} dr \sqrt{2\mu \left(\frac{\kappa}{r} - \lambda r \cos \theta - \mathcal{E} \right)}, \quad (27)$$

where the integration limits were chosen again to ensure exponential decay in the end. The relevant integral is evaluated numerically using Clenshaw-Curtis quadrature.

ITM. With our new potential $V_E(r) = \kappa/r - \lambda r \cos \theta$, our classical sub-barrier equation of motion becomes

$$\mu \ddot{r}(\tau) = -\frac{\kappa}{r^2(\tau)} - \lambda \cos \theta, \quad (28)$$

which is readily solved using any conventional ODE solver. To calculate the static-field transparency we calculate

$$\text{Im } \mathcal{S}_E = \int_0^{\tau_E} d\tau \left[\frac{\mu}{2} \left(\frac{dr(\tau)}{d\tau} \right)^2 + V_E - \mathcal{E} \right], \quad (29)$$

along the solution of Eq. (28).

As for a *dynamic* external electric field, the time dependence of the external laser field is assumed to be harmonic throughout this work, i.e.,

$$V_\omega(r, t) = \frac{\kappa}{r} - \lambda r \cos \theta \cos(\omega t + \varphi), \quad (30)$$

where ω is the angular photon frequency and φ denotes the phase of the electric field. In Sec. III D we will briefly comment on other temporal profiles. As was mentioned previously, we are only considering the ITM for the dynamic case. To calculate the dynamic-field transparency with the ITM, $\mathcal{T}_\omega = \exp(-2 \text{Im } \mathcal{S}_\omega/\hbar)$, we wish to calculate

$$\text{Im } \mathcal{S}_\omega = \int_0^{\tau_\omega} d\tau \left[\frac{\mu}{2} \left(\frac{dr(\tau)}{d\tau} \right)^2 + V_\omega(\tau) - \mathcal{E} \right], \quad (31)$$

with $V_\omega(\tau) = \kappa/r - \lambda r \cos \theta \cos \varphi \cosh(\omega\tau)$ and where, as before, the trajectory along which we integrate is the solution to the sub-barrier equation of motion:

$$\mu \ddot{r}(\tau) = -\frac{\kappa}{r^2(\tau)} - \lambda \cos \theta \cosh(\omega\tau) \cos \varphi. \quad (32)$$

With the entire theoretical framework laid out, we are in a position to discuss all approximations and restrictions that are imposed in the next section.

E. Applicability of semiclassical approaches

In order to use the semiclassical approaches elaborated on in the prior sections, the following necessary restrictions are required:

- (1) The imaginary part of the action in the transparency exponent must be much larger than \hbar , as a consequence of Eq. (8):

$$\text{Im } \mathcal{S} \gg \hbar. \quad (33)$$

Practically, the more lax restriction of $\text{Im } \mathcal{S} > \hbar$ is employed.

- (2) The classical turning point must always be larger than R .
- (3) The use of a one-particle Schrödinger equation neglects all kinds of initial correlation effects between the fusing particles, as well as relativistic effects.
- (4) The presence of the external electric field is modeled using the dipole approximation, for which the wavelength of the laser must be much larger than the spatial extent of the system under consideration, i.e., $\lambda_{\text{laser}} \gg |R_E - R|$.
- (5) The definition of \mathcal{E} remains unaltered when considering an external electric field.
- (6) The parametrized version of the astrophysical S factor is limited to a certain range of CoM energies [47]. In addition, it is assumed that an external electric field does not affect this term.

For the field-free case, we need not be concerned with the dipole approximation. The other points above limit the range for allowable CoM energies to $\mathcal{E} \in [0.3, 183]$ keV and $\mathcal{E} \in [0.5, 66.8]$ keV for DHe³ and DT fusion, respectively. The low values for the upper limit stem from the first point in

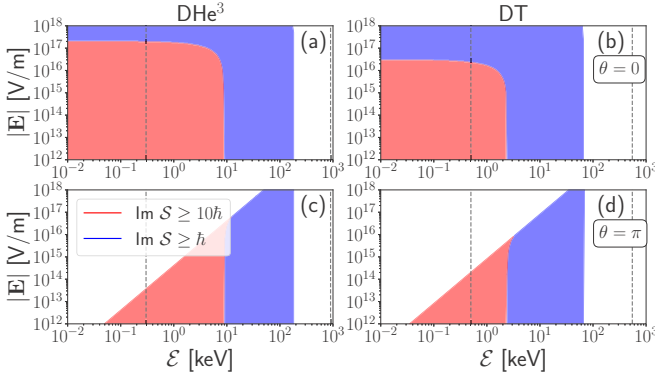


FIG. 3. The region in phase space (\mathcal{E} , $|\mathbf{E}|$) for which the semiclassical approaches in this paper are valid in the static case for DHe^3 fusion [(a),(c)] and DT fusion [(b),(d)], at $\theta = 0$ [(a),(b)] and $\theta = \pi$ [(c),(d)]. Allowed pairs of (\mathcal{E} , $|\mathbf{E}|$) are shown by the colored regions, where the red region denotes the stricter restriction of $\text{Im } S \geq 10\hbar$ as opposed to the more lax $\text{Im } S \geq \hbar$ used elsewhere. The large reduction to the allowable region of phase space at $\theta = \pi$ comes from the breakdown of the dipole approximation when $\cos \theta < 0$ and already occurs at, for instance, $(\mathcal{E}, |\mathbf{E}|) = (1 \text{ keV}, 10^{15} \text{ V/m})$ for both systems.

keeping $\text{Im } S > \hbar$. If we impose the more strict $\text{Im } S > 10\hbar$, these ranges are reduced dramatically to $\mathcal{E} \in [0.3, 8.75] \text{ keV}$ and $\mathcal{E} \in [0.5, 2.35] \text{ keV}$, respectively.

When considering an electric field, we need a value for the laser wavelength λ_{laser} in the condition $\lambda_{\text{laser}} \gg |R_E - R|$, which is practically handled with $\lambda_{\text{laser}} \geq 10|R_E - R|$. The wavelength λ_{laser} is easily related to the photon energy $\hbar\omega$ in the dynamic case. However, when considering a static electric field, we have no such parameter ω . In that case, we account for the dipole approximation as follows. The static-field results are still applicable to a dynamic scenario so long as the timescale of the laser field is much larger than the timescale of the tunneling process. From the trajectories found with the ITM, this tunneling timescale was found to be of the order of 10 as or smaller. Thus, our static-field results are still applicable to dynamic laser fields on a timescale of around 100 as or longer, corresponding to photon energies up to $\hbar\omega \approx 41 \text{ eV}$. This in turn sets a lower limit on λ_{laser} of 30 nm. Thus, for a static field, we practically used $3 \text{ nm} \geq |R_E - R|$ to account for the dipole approximation.

We show the allowed region in phase space (\mathcal{E} , $|\mathbf{E}|$) imposed by the aforementioned approximations and conditions for the two extreme cases of $\theta = 0$ and $\theta = \pi$ in the static-field case in Fig. 3. An upper limit on the electric-field strength is placed at the Schwinger limit of $|\mathbf{E}| = 10^{18} \text{ V/m}$, near which spontaneous pair production is expected to substantially occur. The colored regions denote allowed pairs of (\mathcal{E} , $|\mathbf{E}|$), where the red region denotes the stricter restriction of $\text{Im } S \geq 10\hbar$ as opposed to the more lax $\text{Im } S \geq \hbar$ used elsewhere. The region enclosed by the vertical dashed lines denote those values of \mathcal{E} for which the S -factor parametrization of Bosch and Hale [47] is valid. Worthy of note is that the transition between the forms of the two rows in Fig. 3 is not continuous. A sudden change occurs as θ varies between the

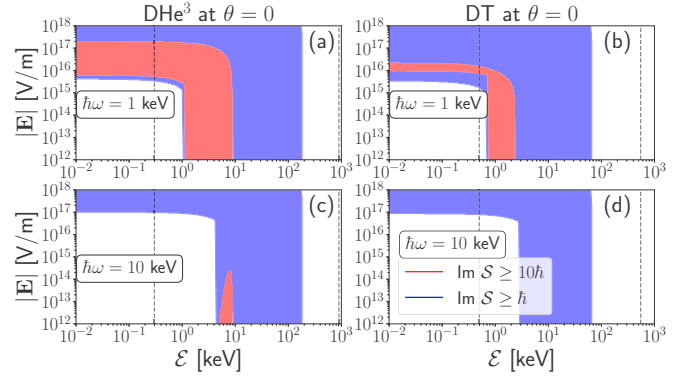


FIG. 4. The region in phase space (\mathcal{E} , $|\mathbf{E}|$) for which the semiclassical approaches in this paper are valid for DHe^3 fusion [(a), (c)] and DT fusion [(b), (d)], at $\hbar\omega = 1 \text{ keV}$ [(a), (b)] and $\hbar\omega = 10 \text{ keV}$ [(c), (d)], with $\theta = 0$ and $\varphi = 0$. Allowed pairs of (\mathcal{E} , $|\mathbf{E}|$) are shown by the colored regions, where the red region denotes the stricter restriction of $\text{Im } S \geq 10\hbar$ as opposed to the more lax $\text{Im } S \geq \hbar$ used elsewhere. The region of phase space where the semiclassical methods are valid is seen to diminish for increasing $\hbar\omega$.

cases of $\cos \theta > 0$, $\cos \theta = 0$, and $\cos \theta < 0$, whereas keeping the sign of $\cos \theta$ fixed and varying θ accounts for small but continuous changes. For $\cos \theta = 0$ the shapes of course revert to rectangles with the red and blue widths ranging from 0.3 to 8.75 keV and from 8.75 to 183 keV for DHe^3 , and from 0.5 to 2.35 keV and from 2.35 to 550 keV for DT.

A plot similar to Fig. 3 is shown for the dynamic case with $\hbar\omega = 1 \text{ keV}$ and $\hbar\omega = 10 \text{ keV}$ at $\theta = 0$ and $\varphi = 0$ in Fig. 4. One can see the vast reduction of allowed phase space as compared to the static case, which becomes worse for higher values of $\hbar\omega$. This is mainly attributed to a breakdown of the dipole approximation in the affected regions. Note that from the relation $\mathcal{T} = \exp(-2 \text{Im } S/\hbar)$ an enhancement to the transparency is captured by a reduction in $\text{Im } S$. Thus, when attempting to capture this enhancement by means of semiclassical methods, for which one inherently requires $\text{Im } S \gg \hbar$, one will inevitably encounter scenarios where the predictions are no longer within their realm of applicability.

III. RESULTS

In this section we calculate the modification to the transparency as a result of a static and a dynamic external electric field and determine their effects on the fusion cross section and reactivity.

A. Static-field enhancement

The values for $\text{Im } S_E$ at $\theta = 0$ in the WKB method and with ITM are compared to each other in Fig. 5. The value of $\hbar = 0.6582 \text{ eV fs}$ is also shown to illustrate $\text{Im } S_E > \hbar$. One can see that the WKB (lines) and the ITM (dots) results practically overlap. Note that a lower value of $\text{Im } S_E$ denotes a larger enhancement to the transparency. We emphasize that the scales on the y axes in Fig. 5 differ between the DHe^3 and DT results. This is done for aesthetic reasons to showcase

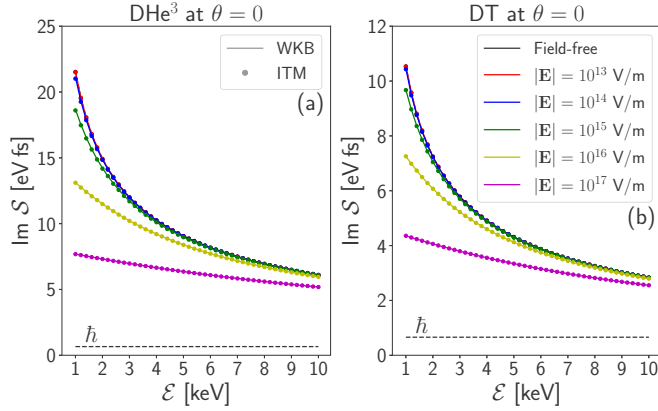


FIG. 5. The static-field value of $\text{Im } S_E$ at $\theta = 0$ for DHe^3 (a) and DT (b) at electric-field strengths $|\mathbf{E}| = 10^{13}$ V/m to $|\mathbf{E}| = 10^{17}$ V/m. The lines and dots refer to the WKB and ITM result respectively. Also shown are the field-free values ($|\mathbf{E}| = 0$ V/m) and the value of $\hbar = 0.6582$ eV fs (black dotted line). Note that the scales on the y axes differ and that the two legends refer to both plots simultaneously. A reduction in $\text{Im } S_E$ signifies enhancement with respect to the field-free case, which starts to set in for both systems at $|\mathbf{E}| > 10^{14}$ V/m and is more prominent for lower values of \mathcal{E} .

the DT results more clearly. In addition, the two legends refer to both plots simultaneously. We will adhere to similar conventions for all subsequent figures in this paper. One can conclude from Fig. 5 that nearly no enhancement is present for electric-field strengths below a certain critical value, which echoes the conclusions of Queisser and Schützhold [32], Lv *et al.* [33], and Liu *et al.* [36]. An important observation from Fig. 5 is that this critical field value depends on \mathcal{E} . For low values of \mathcal{E} enhancement appears to set in for both systems at $|\mathbf{E}| > 10^{14}$ V/m. However, at higher values for \mathcal{E} , the enhancement appears to wane, which is partly why we do not show higher \mathcal{E} values than 10 keV. This trend is also present in the works of Wang [34] and Liu *et al.* [36]. Lastly, note that the enhancement is more prominent for DHe^3 than it is for DT . We expect this to be a consequence of the fact that the product $Z_1 Z_2$ is larger for DHe^3 ($Z_1 Z_2 = 2$) than for DT ($Z_1 Z_2 = 1$) for the following reason. As the Coulomb repulsion in DHe^3 is larger than in DT , the field-free classical turning point R_E is also larger for DHe^3 than for DT , when considering the same CoM energy \mathcal{E} . From Fig. 2 it is clear that an external laser field deforms the potential more drastically further away in the tail, rather than close to the origin. Hence, the inclusion of the external laser field reduces the classical turning point much more in the case of DHe^3 than in DT and thus causes a more pronounced enhancement to the former. Therefore, even though a larger Coulomb repulsion would hinder a typical fusion process, we conclude that the laser-induced enhancement is actually larger in this case.

Figure 6 shows the effect of a static electric field on the fusion cross sections. Again, any enhancement appears to be most prominent for lower values of \mathcal{E} . By considering a specific CoM value, e.g., $\mathcal{E} = 1$ keV, we can highlight vast enhancements to the cross section when considering the ambitious, but realistic, field strengths of $|\mathbf{E}| = 10^{15}$ V/m and

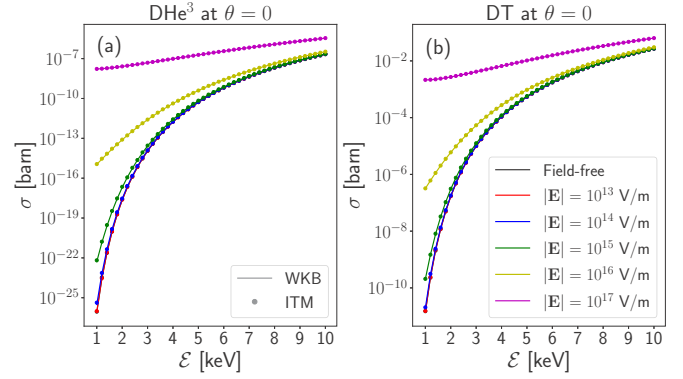


FIG. 6. The static-field cross section at $\theta = 0$ for DHe^3 (a) and DT (b) at electric-field strengths $|\mathbf{E}| = 10^{13}$ V/m to $|\mathbf{E}| = 10^{17}$ V/m. The lines and dots refer to the WKB and ITM result respectively, which are seen to agree well with one another. Additionally, the field-free values practically overlap with the results for $|\mathbf{E}| = 10^{13}$ V/m. One can see noticeable enhancements for $|\mathbf{E}| > 10^{14}$ V/m, which are more prominent for lower values of \mathcal{E} .

$|\mathbf{E}| = 10^{16}$ V/m. These enhancements are six to eleven orders of magnitude for DHe^3 fusion and one to four orders of magnitude for DT fusion. However, Fig. 6 illustrates that these large enhancements do not persist for most CoM energies. The resulting effect on the reactivity is shown in Fig. 7, given a thermal Maxwellian velocity distribution. The cutoffs for the energy integral were 183 and 66.8 keV for DHe^3 and DT respectively, corresponding to the largest shown values for the temperatures at $k_B T = 72$ keV and $k_B T = 31$ keV. The reactivity plots show that the enhancement to the cross sections is not enough to result in an overall effect when integrating over \mathcal{E} , with the extreme case of $|\mathbf{E}| = 10^{17}$ V/m being the exception. We note that even though the absolute values for the reactivity may be rather crude, regarding the used approximation of a thermal Maxwellian velocity distribution, the relative enhancement in the reactivity between different

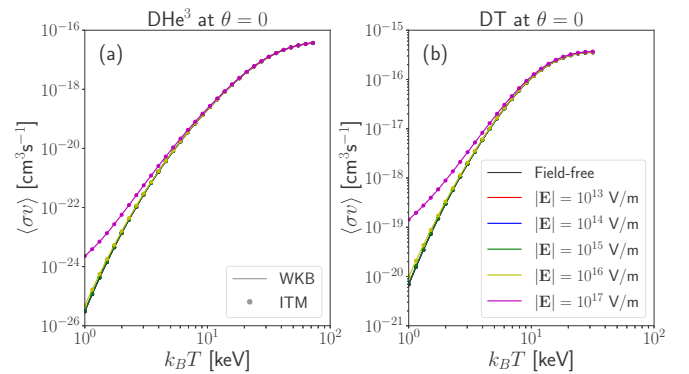


FIG. 7. The static-field reactivity at $\theta = 0$ for DHe^3 (a) and DT (b) at electric-field strengths $|\mathbf{E}| = 10^{13}$ V/m to $|\mathbf{E}| = 10^{17}$ V/m. The solid lines and dots refer to the WKB and ITM result respectively. Also shown are the field-free values. The large laser-induced enhancements to the cross section are seen to have a lasting impact only for the most extreme values of $|\mathbf{E}|$.

values for the electric-field strength $|\mathbf{E}|$ does not depend on this choice. Based on the prediction from the transparency and cross section calculations, a noticeable enhancement will only be present for a relatively small range of CoM energies, at least for $|\mathbf{E}|$ values that are attainable at present-day facilities ($<10^{16}$ V/m). Subsequently, an overall enhancement in the reactivity as a result of the potential deformation alone is not expected to appear. We do note that Fig. 7 depicts a log-log plot, so enhancements below an order of magnitude, though present, are hardly discernible. For example, the enhancements to the reactivity at $k_B T = 1$ keV for $|\mathbf{E}| = 10^{16}$ V/m are factors of 1.67 and 1.43 for DHe^3 and DT respectively.

The question remains whether or not the estimates for the transparency enhancements may have been underestimated regarding the use of the semiclassical methods. Despite the results presented thus far being within their realm of applicability, the WKB method for example is well known to deteriorate in accuracy as \mathcal{E} decreases. For CoM energies far below the largest potential values of the barrier, the WKB method can underestimate the transparency predictions by several orders of magnitude [9]. The use of semiclassical approaches would be unwarranted if unphysical results can be encountered even in the regime where the employed approach fulfills the validity requirements. We return to this point in Sec. III D when considering the dynamic-field case. Let us first comment on the effect of the polarization angle θ in a more realistic setting.

B. Polarization angle averaging

The angle between the relative movement of fusing particles and the polarization direction of the external laser field will be, to a large degree, random in a real experiment. The results presented thus far were given in the best-case scenario of maximal enhancement at $\theta = 0$. However, suppression is expected to occur for those angles with $\cos \theta < 0$, as is intuitively clear from Fig. 2. Therefore, we must average over the angle θ to determine whether any enhancement remains in a real experimental setting. The averaging is done with respect to the cross section as

$$\sigma_{\text{ave}}(\mathcal{E}, |\mathbf{E}|) = \frac{1}{2} \int_0^\pi d\theta \sigma(\mathcal{E}, |\mathbf{E}|, \theta) \sin \theta. \quad (34)$$

However, recall that cases exist with $\cos \theta < 0$ for which there is no more tunneling possible, which was an artifact from using the dipole approximation where we ought not to. How should this be handled during the averaging? Simply equaling $\sigma(\mathcal{E}, |\mathbf{E}|, \theta) = 0$ in that case will artificially skew the average towards an overall smaller enhancement. To avoid this, we will only show averaged cross section values at those values of $(\mathcal{E}, |\mathbf{E}|)$ for which all values of $\theta \in [0, \pi]$ provided a physical result. These are shown as dots in Fig. 8 for electric-field strengths from $|\mathbf{E}| = 10^{13}$ V/m to $|\mathbf{E}| = 10^{17}$ V/m. The lines in Fig. 8 refer to the WKB result for the cross section at the fixed angle of $\theta = 0$. One can see that, even when averaging over polarization directions, an overall enhancement is still expected to arise in the static-field case, albeit by a much smaller amount as compared to $\theta = 0$. Also, the amount of points for which data can be acquired is heavily limited.

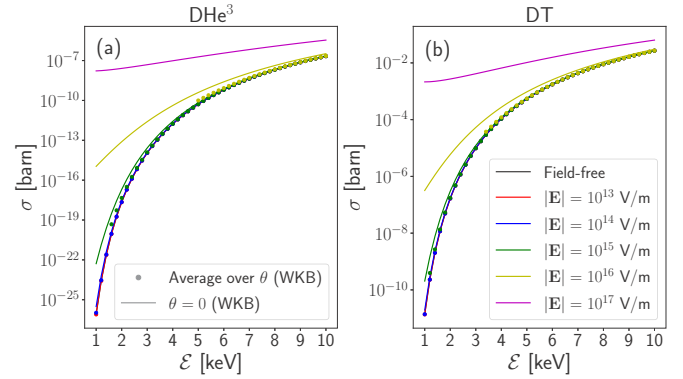


FIG. 8. The static-field cross sections (WKB result) for DHe^3 (a) and DT (b) at electric-field strengths $|\mathbf{E}| = 10^{13}$ V/m to $|\mathbf{E}| = 10^{17}$ V/m. The lines and dots refer to the cases of $\theta = 0$ and averaged over θ , respectively. Averaged values are only shown if all $\theta \in [0, \pi]$ provided physical answers for a given set of input parameters. Though the θ -averaged cross section is found to be generally smaller than the cross section at $\theta = 0$, an overall net enhancement can still be observed in the former case.

We now turn to comparing these results with other theoretical predictions from the literature.

C. Theoretical predictions comparison: Static

The large majority of works in the literature have employed the use of the velocity gauge and therefore consider the frequency, and consequent photon energy, of the laser field as a parameter in their enhancement estimates. As our field is static, we have no such parameter. However, we noted before that the static-field results are still applicable to a dynamic scenario for photon energies up to $\hbar\omega \approx 40$ eV.

The work of Wang [34] considered the effect of near-infrared lasers on DT fusion. They predicted an enhancement to the θ -averaged DT fusion cross section of nine orders of magnitude at $\mathcal{E} = 1$ keV for an 800-nm laser ($\hbar\omega = 1.55$ eV) at $I = 5 \times 10^{21}$ W/cm² ($|\mathbf{E}| = 2 \times 10^{14}$ V/m). At $\mathcal{E} = 5$ keV and $\mathcal{E} = 10$ keV for the same laser parameters their enhancement was two orders of magnitude and one order of magnitude, respectively. However, for the same parameters we predict an enhancement by factors of 1.135, 1.006, and 1.002, respectively. The discrepancy between our results and those of Wang stems from the fact that the Coulomb barrier is ignored in Ref. [34], which is incidentally mentioned as a similar cause for discrepancy in Ref. [36].

Next, we consider the work of Liu *et al.* [36], which considers DT fusion using the WKB method. The difference with the current work is that the classical turning point is not determined analytically, but rather determined from a Monte Carlo sampling of many classical prebarrier trajectories of a Gaussian wave packet. At $\mathcal{E} = 1$ keV and $\hbar\omega = 1$ eV they see θ -averaged cross section enhancements occur at intensities $I = 10^{20}$ W/cm², $I = 10^{21}$ W/cm², and $I = 10^{22}$ W/cm² by 3, 6, and 7 orders of magnitude, respectively. At those same parameters, we found enhancements by factors of 1.0701, 1.0866, and 1.2166, respectively. The discrepancy may be

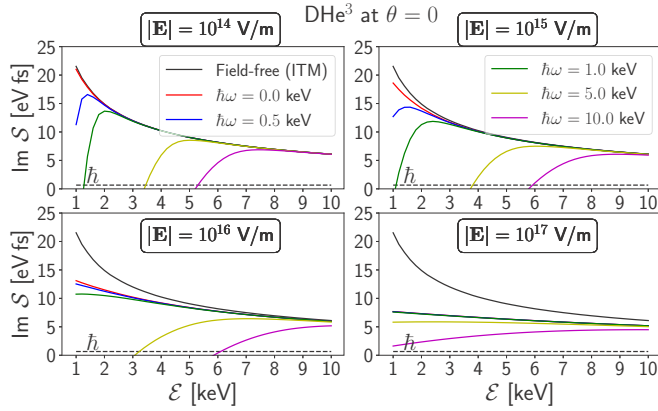


FIG. 9. The dynamic-field enhanced results for $\text{Im } S_\omega$ as a function of the CoM energy \mathcal{E} , calculated by the ITM at $\theta = 0$ for DHe^3 at electric-field strengths $|\mathbf{E}| = 10^{14}$ V/m to $|\mathbf{E}| = 10^{17}$ V/m and various photon energies $\hbar\omega$. A larger enhancement is expected for higher $\hbar\omega$. However, this enhancement can be unphysically large, especially for lower values of $|\mathbf{E}|$, showcasing the reduced applicability of the semiclassical methods at increasing $\hbar\omega$.

caused by the use of a time-dependent potential in the inherently time-independent WKB expression for the transparency [Eqs. (9) and (10)] in Ref. [36], though admittedly it is not explicitly mentioned how the time dependence is handled. We discuss their dynamic enhancement predictions in Sec. III F.

We now proceed by considering the enhancement due to dynamic external electric fields.

D. Dynamic-field enhancement

In this section, we assume $\theta = 0$ and $\varphi = 0$. An averaging over the phase angle φ is briefly addressed in Sec. III E. Figure 9 shows $\text{Im } S_\omega$ as a function of the CoM energy \mathcal{E} for DHe^3 fusion. Each panel denotes a different electric-field strength, ranging from $|\mathbf{E}| = 10^{14}$ V/m to $|\mathbf{E}| = 10^{17}$ V/m, and shows the results for different values of $\hbar\omega$ at a given field strength. The results from Fig. 9 show an increased enhancement for increasing photon energy $\hbar\omega$ as compared to the static-field case (consistently shown as the red curve in this section), most prominently for higher values of $|\mathbf{E}|$ and again for lower values of \mathcal{E} . However, Fig. 9 reveals a worrying trend, as for higher values of $\hbar\omega$ the values of $\text{Im } S_\omega$ may be of the order of and even far below \hbar , whereas the ITM is only valid in the limit of $\text{Im } S_\omega \gg \hbar$. The sudden drop in $\text{Im } S_\omega$ for decreasing values of \mathcal{E} are undoubtedly unphysical, as they lead to enormous enhancements in the cross section, shown in Fig. 10. And this despite being in the range of applicability of semiclassical methods. The results indicate that the range of applicability of the ITM in the dynamic case is more restricted for low electric-field strengths. In the case of $|\mathbf{E}| = 10^{17}$ V/m all values of $\text{Im } S_\omega$ are larger than \hbar for all $\hbar\omega$. For the cross sections in Fig. 10, the solid lines refer to the results obtained from the transparency shown in Fig. 9. The dots refer to cross section results obtained with the much more strict requirement of $\text{Im } S_\omega > 10\hbar$ to determine if the unphysical exponential enhancement at low \mathcal{E} disappears.

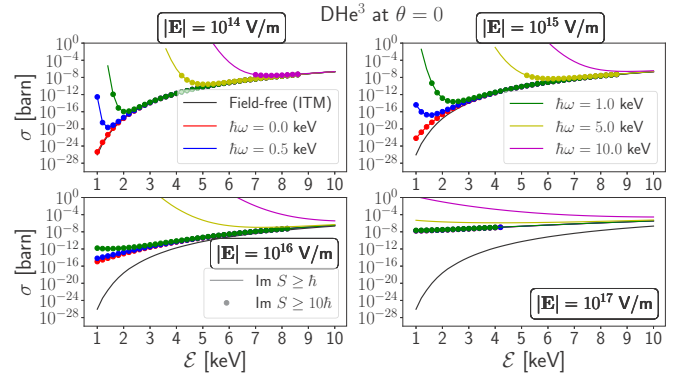


FIG. 10. The dynamic-field enhanced cross section as a function of the CoM energy \mathcal{E} , calculated by the ITM at $\theta = 0$ for DHe^3 , at electric-field strengths $|\mathbf{E}| = 10^{14}$ V/m to $|\mathbf{E}| = 10^{17}$ V/m and photon energies $\hbar\omega$. The lines refer to results obtained from the requirement that $\text{Im } S_\omega > \hbar$ and the dots were obtained using the more strict requirement $\text{Im } S_\omega > 10\hbar$. One can see that the unphysical enhancements that arose from the rapidly decreasing values of $\text{Im } S_\omega$ with decreasing \mathcal{E} (Fig. 9) persist in the cross section, even when $\text{Im } S_\omega > 10\hbar$.

However, Fig. 10 shows that it may persist even then, especially at lower values of $|\mathbf{E}|$. The inevitable conclusion is that the dynamic-field enhancement cannot be suitably described by semiclassical approaches. The region of phase space that gives accurate results is far too restricted to be able to provide reactivity estimates and thus they are not presented here. The results for $\text{Im } S_\omega$ for DT fusion largely mimic the behaviors of Figs. 9 and are omitted for this reason. The dynamically enhanced fusion cross section for DT is presented in Fig. 11 for completeness.

Temporal profiles other than a harmonic one were also considered. Similar to Ref. [32], we considered a Gaussian pulse and a de Sauter pulse, where the time dependence is changed

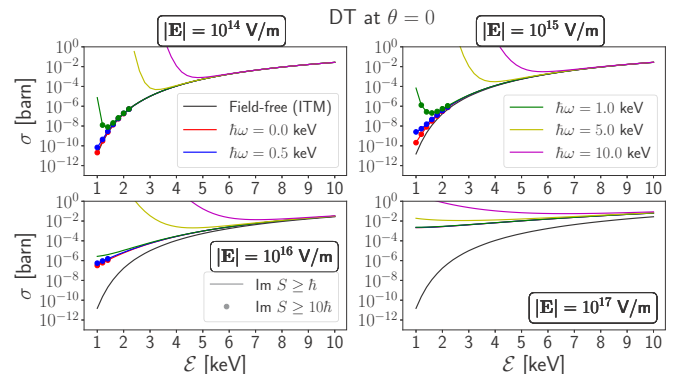


FIG. 11. The dynamic-field enhanced cross section as a function of the CoM energy \mathcal{E} , calculated by the ITM at $\theta = 0$ for DT, at electric-field strengths $|\mathbf{E}| = 10^{14}$ V/m to $|\mathbf{E}| = 10^{17}$ V/m and various photon energies $\hbar\omega$. The solid lines refer to results obtained from the requirement that $\text{Im } S_\omega > \hbar$ and the dots were obtained using the more strict requirement $\text{Im } S_\omega > 10\hbar$. The behavior from Fig. 10 is largely mimicked.

from $\cos(\omega t)$ to $\exp\{-(\omega t)^2\}$ and $1/\cosh^2(\omega t)$ respectively. Unfortunately, the only differences we saw to the enhanced cross sections in these cases were in regions where the results showed the unphysically large artifacts. For this reason, we omitted these plots.

E. Phase angle averaging

The final parameter to model the external laser field left to discuss is the phase angle present in the time dependence as $\cos(\omega t + \varphi)$. Assuming φ to be a constant, we may assign its value to the one at $t = 0$ and average the cross section from $\varphi = 0$ to $\varphi = 2\pi$ as

$$\sigma_{\text{ave}}(\mathcal{E}, |\mathbf{E}|, \theta, \omega) = \frac{1}{2\pi} \int_0^{2\pi} d\varphi \sigma(\mathcal{E}, |\mathbf{E}|, \theta, \omega, \varphi). \quad (35)$$

Note that the phase-angle averaging introduces a degree of incoherence into the laser field. Unfortunately, a similar conclusion was found as when different temporal profiles were considered. Namely, the only differences that were observed between the φ -averaged case and $\varphi = 0$ were in regions where the enhancements were unphysical. Therefore, these plots were omitted as well. However, for those parameters where the results did appear physically justifiable, we could hardly discern a difference between the phase-averaged results and the field-free results. This is in disagreement with the conclusion presented by Queisser and Schützhold [32] that dynamic enhancement will also occur with incoherent light sources. However, a definite answer to this question would be provided given accurate dynamic cross-section enhancements for lower values of \mathcal{E} , which is unfortunately not possible within the semiclassical approximation.

F. Theoretical predictions comparison: Dynamic

Despite the limited range of applicability of the ITM in the dynamic case, we may compare our enhancement results for DT fusion with other theoretical works.

The work of Queisser and Schützhold [32] predicts significant enhancement to the transparency for $\mathcal{E} = \hbar\omega = 1$ keV, provided either $|\mathbf{E}| = 10^{13}$ V/m or $|\mathbf{E}| = 10^{15}$ V/m, depending on the method employed. It is not stated what is meant with “significant,” but with the dynamic-field calculation using the ITM we found enhancements to the cross section at $\mathcal{E} = 1$ keV and $|\mathbf{E}| = 10^{13}$ V/m by a factor of 50 and a factor of $\approx 5 \times 10^6$ for $|\mathbf{E}| = 10^{15}$ V/m. However, these large enhancements are unphysical as evidenced by Fig. 11. Realistic enhancement factors are likely to be much smaller. Queisser and Schützhold also predict a significant enhancement factor can be seen at $\mathcal{E} = 9$ keV and $\hbar\omega = 27$ keV for electric-field strengths below $|\mathbf{E}| = 10^{13}$ V/m. We predict at $\mathcal{E} = 9$ keV, $\hbar\omega = 27$ keV, and $|\mathbf{E}| = 10^{13}$ V/m an enhancement factor to the cross section of 1.024. However, Queisser and Schützhold did mention their predictions are less reliable in this regime.

The work of Lv *et al.* [33] makes predictions for the DT fusion cross section enhancement using the Kramers-Henneberger (KH) approximation, which is applicable if the time period of the laser is much smaller than the time scale of the fusion process. It is stated that their method is ap-

TABLE I. Predictions for the enhancement factor to the cross section using the dynamic-field ITM at laser parameters that correspond to $n_d = 9$ in Ref. [33] at $\mathcal{E} = 64$ keV. Also shown are the values for $\text{Im } S/\hbar$. We find hardly any enhancement occurs at these values, mainly attributed to the consideration of the relatively high value of $\mathcal{E} = 64$ keV.

$\hbar\omega$ (keV)	$ \mathbf{E} $ (V/m)	$\sigma_\omega/\sigma_{\mathcal{E}}$	$\text{Im } S_\omega/\hbar$
1.0	5.059×10^{15}	1.0008	1.0445
2.5	3.162×10^{16}	1.0037	1.0431
5.0	1.265×10^{17}	1.0143	1.0378
7.5	2.846×10^{17}	1.0318	1.0292
10.0	5.059×10^{17}	1.0561	1.0176

pllicable for $\hbar\omega \geq 1$ keV. Predictions are made with respect to the dimensionless parameter $n_d = e\sqrt{2c\mu_0 I}/(5\mu\omega^2 R)$, which, with the intensity being $I = c\epsilon_0|\mathbf{E}|^2/2$, becomes $n_d = e|\mathbf{E}|/(5\mu\omega^2 R)$. A single value of n_d defines a curve in the $(|\mathbf{E}|, \hbar\omega)$ plane consistent of pairs that lead to the same enhancement. At $\mathcal{E} = 64$ keV and $n_d = 9$, they predicted an enhancement to the θ -averaged cross section by a factor of 4.77. For a handful of photon energies in the keV regime and corresponding electric-field strengths that satisfy the relation $n_d = 9$, we show our dynamic-field enhancement to the cross section at $\mathcal{E} = 64$ keV in Table I. Nearly no enhancement is predicted for any of the suggested parameters, as it was shown for the enhancements to be most prevalent for low values of \mathcal{E} in the ITM. Interestingly, this illustrates a qualitative difference between the results of the ITM and KH approximation, again showcasing the need for experimental validation.

Finally, we reconsider the work of Liu *et al.* [36], which also made predictions to the DT fusion θ -averaged cross section enhancement at a photon energy of $\hbar\omega = 1$ keV. For this value, and with $\mathcal{E} = 1$ keV and $I = 10^{26}$ W/cm², $I = 10^{27}$ W/cm², and $I = 10^{28}$ W/cm², they find enhancements by factors of ≈ 5 , 10^2 , and 10^5 , respectively. These parameters unfortunately lie outside of the validity range of our approach.

The vast differences in theoretical predictions for the enhancements come from the fact that the laser-induced enhancement does not set in until some critical value for the electric-field strength is reached. As different models predict different critical values, their enhancement predictions may indeed differ by several orders of magnitude. This was already shown in Fig. 5 of Liu *et al.* [36], which compares their work with Lv *et al.* [33] and Wang [34]. A similar critical photon energy is also expected to exist, as mentioned by Queisser and Schützhold [32], but could not be determined due to the restricted applicability of semiclassical methods in this work.

IV. CONCLUSIONS AND OUTLOOK

In this paper, we have employed two frequently used semiclassical approaches, the WKB method and the ITM, to calculate the enhancement in the fusion rates expected to arise from an external laser field, for the cases of DHe³ and DT fusion. The goals were to go beyond a simple prediction of enhancement at a few select CoM energies and laser parameters in order to provide a more accurate and realistic enhancement

prediction that is to be expected during a real experiment, and to determine whether semiclassical approaches are capable of doing so. The conclusion is that a large range of input parameters is necessary to make accurate predictions similar to an experiment and that semiclassical approaches are not applicable for the entire necessary region in phase space. Especially the combination of small $|E|$ and large $\hbar\omega$ hinders the use of these methods. Furthermore, even where the semiclassical approaches ought to be valid, the predicted result may still diverge at low CoM energies in the dynamic case.

With the purpose of actually designing a laser-enhanced fusion experiment, the optimal laser parameters will most accurately be found by going beyond semiclassical methods. The KH approximation is an excellent start to consider the enhancement at high $\hbar\omega$, but the method seems to indicate larger enhancements for lower values of $\hbar\omega$ [33,37], where

the method is less accurate. A connection can be made to the low- $\hbar\omega$ regime by extending the framework presented in Ref. [34] to include a Coulomb-Volkov state. Alternatively, the R -matrix method may be employed to calculate the transparency, similar to what was done in Ref. [54]. A benchmark can be made with the transparency calculated from the full numerical solution of the time-dependent Schrödinger equation. This development is currently underway.

ACKNOWLEDGMENTS

The authors would like to express their gratitude to Christian Bild for fruitful discussions. The work by SLAC HED division is supported by DOE Office of Science, Fusion Energy Science under FWP 100182. M.L.L. acknowledges support by the National Science Foundation MPS AGEP Graduate Research Supplement.

-
- [1] B. Bishop, National Ignition Facility experiment puts researchers at threshold of fusion ignition, Lawrence Livermore National Laboratory News, August 2021, <https://www.llnl.gov/news/national-ignition-facility-experiment-puts-researchers-threshold-fusion-ignition>
- [2] A. B. Zylstra, O. A. Hurricane, D. A. Callahan, A. L. Kritcher, J. E. Ralph, H. F. Robey, J. S. Ross, C. V. Young, K. L. Baker, D. T. Casey *et al.*, Burning plasma achieved in inertial fusion, *Nature (London)* **601**, 542 (2022).
- [3] A. L. Kritcher, C. V. Young, H. F. Robey, C. R. Weber, A. B. Zylstra, O. A. Hurricane, D. A. Callahan, J. E. Ralph, J. S. Ross, K. L. Baker *et al.*, Design of inertial fusion implosions reaching the burning plasma regime, *Nat. Phys.* **18**, 251 (2022).
- [4] F. Hund, Zur Deutung der Molekelspektren. I, *Z. Phys.* **40**, 742 (1927).
- [5] F. Hund, Zur Deutung der Molekelspektren. II, *Z. Phys.* **42**, 93 (1927).
- [6] F. Hund, Zur Deutung der Molekelspektren. III, *Z. Phys.* **43**, 805 (1927).
- [7] G. Gamow, Zur Quantentheorie des Atomkernes, *Z. Phys.* **51**, 204 (1928).
- [8] R. W. Gurney and E. U. Condon, Quantum Mechanics and Radioactive Disintegration, *Phys. Rev.* **33**, 127 (1929).
- [9] J. M. Blatt and V. F. Weisskopf, *Theoretical Nuclear Physics*, 2nd ed. (Springer-Verlag, New York, 1979).
- [10] D. D. Clayton, *Principles of Stellar Evolution and Nucleosynthesis*, 2nd ed. (University of Chicago Press, Chicago, 1983).
- [11] F. L. Hinton and R. D. Hazeltine, Theory of plasma transport in toroidal confinement systems, *Rev. Mod. Phys.* **48**, 239 (1976).
- [12] J. Sheffield, The physics of magnetic fusion reactors, *Rev. Mod. Phys.* **66**, 1015 (1994).
- [13] J. Ongena, R. Koch, R. Wolf, and H. Zohm, Magnetic-confinement fusion, *Nat. Phys.* **12**, 398 (2016).
- [14] J. Nuckolls, L. Wood, A. Thiessen, and G. Zimmerman, Laser compression of matter to super-high densities: Thermonuclear (CTR) applications, *Nature (London)* **239**, 139 (1972).
- [15] J. Lindl, Development of the indirect-drive approach to inertial confinement fusion and the target physics basis for ignition and gain, *Phys. Plasmas* **2**, 3933 (1995).
- [16] S. Atzeni and J. Meyer-ter-Vehn, *The Physics of Inertial Fusion: Beam Plasma Interaction, Hydrodynamics, Hot Dense Matter* (Oxford University Press, Oxford, 2004).
- [17] J. D. Lindl, P. Amendt, R. L. Berger, S. G. Glendinning, S. H. Glenzer, S. W. Haan, R. L. Kauffman, O. L. Landen, and L. J. Suter, The physics basis for ignition using indirect-drive targets on the National Ignition Facility, *Phys. Plasmas* **11**, 339 (2004).
- [18] O. A. Hurricane, D. A. Callahan, D. T. Casey, P. M. Celliers, C. Cerjan, E. L. Dewald, T. R. Dittrich, T. Döppner, D. E. Hinkel, L. F. Berzak Hopkins *et al.*, Fuel gain exceeding unity in an inertially confined fusion implosion, *Nature (London)* **506**, 343 (2014).
- [19] R. Betti and O. A. Hurricane, Inertial-confinement fusion with lasers, *Nat. Phys.* **12**, 435 (2016).
- [20] V. S. Popov, Tunnel and multiphoton ionization of atoms and ions in a strong laser field (Keldysh theory), *Phys. Usp.* **47**, 855 (2004).
- [21] S. V. Popruzhenko, Keldysh theory of strong field ionization: history, applications, difficulties and perspectives, *J. Phys. B: At. Mol. Opt. Phys.* **47**, 204001 (2014).
- [22] H. M. Castañeda Cortés, C. Müller, C. H. Keitel, and A. Pálffy, Nuclear recollisions in laser-assisted α decay, *Phys. Lett. B* **723**, 401 (2013).
- [23] Ș. Mișicu and M. Rizea, α -decay in ultra-intense laser fields, *J. Phys. G: Nucl. Part. Phys.* **40**, 095101 (2013).
- [24] Ș. Mișicu and M. Rizea, Speeding of α decay in strong laser fields, *Open Phys.* **14**, 81 (2016).
- [25] D. S. Delion and S. A. Ghinescu, Geiger-Nuttall Law for Nuclei in Strong Electromagnetic Fields, *Phys. Rev. Lett.* **119**, 202501 (2017).
- [26] D. P. Kis and R. Szilvasi, Three dimensional α -tunneling in intense laser fields, *J. Phys. G: Nucl. Part. Phys.* **45**, 045103 (2018).
- [27] D. Bai, D. Deng, and Z. Ren, Charged particle emissions in high-frequency alternative electric fields, *Nucl. Phys. A* **976**, 23 (2018).
- [28] J. Qi, T. Li, R. Xu, L. Fu, and X. Wang, α decay in intense laser fields: Calculations using realistic nuclear potentials, *Phys. Rev. C* **99**, 044610 (2019).

- [29] S. A. Ghinescu and D. S. Delion, Coupled-channels analysis of the α decay in strong electromagnetic fields, *Phys. Rev. C* **101**, 044304 (2020).
- [30] A. Pálffy and S. V. Popruzhenko, Can Extreme Electromagnetic Fields Accelerate the α Decay of Nuclei?, *Phys. Rev. Lett.* **124**, 212505 (2020).
- [31] J. Qi, L. Fu, and X. Wang, Nuclear fission in intense laser fields, *Phys. Rev. C* **102**, 064629 (2020).
- [32] F. Queisser and R. Schützhold, Dynamically assisted nuclear fusion, *Phys. Rev. C* **100**, 041601(R) (2019).
- [33] W. Lv, H. Duan, and J. Liu, Enhanced deuterium-tritium fusion cross sections in the presence of strong electromagnetic fields, *Phys. Rev. C* **100**, 064610 (2019).
- [34] X. Wang, Substantially enhanced deuteron-triton fusion probabilities in intense low-frequency laser fields, *Phys. Rev. C* **102**, 011601(R) (2020).
- [35] C. Kohlfürst, F. Queisser, and R. Schützhold, Dynamically assisted tunneling in the impulse regime, *Phys. Rev. Research* **3**, 033153 (2021).
- [36] S. Liu, H. Duan, D. Ye, and J. Liu, Deuterium-tritium fusion process in strong laser fields: Semiclassical simulation, *Phys. Rev. C* **104**, 044614 (2021).
- [37] W. Lv, B. Wu, H. Duan, S. Liu, and J. Liu, Phase-dependent cross sections of deuteron-triton fusion in dichromatic intense fields with high-frequency limit, *Eur. Phys. J. A* **58**, 54 (2022).
- [38] B. Wu, H. Duan, and J. Liu, Resonant tunneling of deuteron-triton fusion in strong high-frequency electromagnetic fields, [arXiv:2112.12384](https://arxiv.org/abs/2112.12384).
- [39] P. Emma, R. Akre, J. Arthur, R. Bionta, C. Bostedt, J. Bozek, A. Brachmann, P. Bucksbaum, R. Coffee, F.-J. Decker *et al.*, First lasing and operation of an ångstrom-wavelength free-electron laser, *Nat. Photonics* **4**, 641 (2010).
- [40] T. Ishikawa, H. Aoyagi, T. Asaka, Y. Asano, N. Azumi, T. Bizen, H. Ego, K. Fukami, T. Fukui, Y. Furukawa *et al.*, A compact X-ray free-electron laser emitting in the sub-ångström region, *Nat. Photonics* **6**, 540 (2012).
- [41] T. Tschentscher, C. Bressler, J. Grünert, A. Madsen, A. P. Mancuso, M. Meyer, A. Scherz, H. Sinn, and Ulf Zastrau, Photon beam transport and scientific instruments at the European XFEL, *Appl. Sci.* **7**, 592 (2017).
- [42] W. Decking, S. Abeghyan, P. Abramian, A. Abramsky, A. Aguirre, C. Albrecht, P. Alou, M. Altarelli, P. Altmann, K. Amyan *et al.*, A MHz-repetition-rate hard X-ray free-electron laser driven by a superconducting linear accelerator, *Nat. Photonics* **14**, 391 (2020).
- [43] H.-S. Kang, C.-K. Min, H. Heo, C. Kim, H. Yang, G. Kim, I. Nam, S. Y. Baek, H.-J. Choi, G. Mun *et al.*, Hard X-ray free-electron laser with femtosecond-scale timing jitter, *Nat. Photonics* **11**, 708 (2017).
- [44] C. J. Milne, T. Schietinger, M. Aiba, A. Alarcon, J. Alex, A. Anghel, V. Arsov, C. Beard, P. Beaud, S. Bettoni *et al.*, Swiss-FEL: The Swiss X-ray Free Electron Laser, *Appl. Sci.* **7**, 720 (2017).
- [45] V. S. Popov, Imaginary-time method in quantum mechanics and field theory, *Phys. At. Nucl.* **68**, 686 (2005).
- [46] S. H. Glenzer, L. B. Fletcher, E. Galtier, B. Nagler, R. Alonso-Mori, B. Barbrel, S. B. Brown, D. A. Chapman, Z. Chen, C. B. Curry *et al.*, Matter under extreme conditions experiments at the Linac Coherent Light Source, *J. Phys. B: At. Mol. Opt. Phys.* **49**, 092001 (2016).
- [47] H.-S. Bosch and G. M. Hale, Improved formulas for fusion cross-sections and thermal reactivities, *Nucl. Fusion* **32**, 611 (1992).
- [48] D. J. Griffiths, *Introduction to Quantum Mechanics*, 2nd ed. (Pearson Education, Upper Saddle River, NJ, 2005).
- [49] J. J. Sakurai, *Modern Quantum Mechanics*, 2nd ed. (Pearson Education, Upper Saddle River, NJ, 2011).
- [50] L. O’Raifeartaigh and A. Wipf, WKB properties of the time-dependent Schrödinger system, *Found. Phys.* **18**, 307 (1988).
- [51] M. Boiron and M. Lombardi, Complex trajectory method in semiclassical propagation of wave packets, *J. Chem. Phys.* **108**, 3431 (1998).
- [52] Y. Goldfarb, J. Schiff, and D. J. Tannor, Complex trajectory method in time-dependent WKB, *J. Chem. Phys.* **128**, 164114 (2008).
- [53] W. M. Nevins and R. Swain, The thermonuclear fusion rate coefficient for p-¹¹B reactions, *Nucl. Fusion* **40**, 865 (2000).
- [54] G. Hupin, S. Quaglioni, and P. Navratil, Ab initio predictions for polarized deuterium-tritium thermonuclear fusion, *Nat. Commun.* **10**, 351 (2019).